Mechanical control of morphogenesis robustness

One sentence summary: Force channeling ensures morphogenesis robustness in a mechanically noisy environment

Emmanuel Martin[1], Sophie Theis[1,2], Guillaume Gay[2], Bruno Monier[1] and Magali Suzanne[1]

[1] LBCMCP, Centre de Biologie Intégrative (CBI), Université de Toulouse, CNRS, UPS, France

[2] Morphogénie Logiciels, 32110 St Martin d'Armagnac, France

Correspondence: magali.suzanne@univ-tlse3.fr; guillaume@damcb.com;

Abstract

Epithelial sheets undergo highly reproducible remodeling to shape organs. This stereotyped morphogenesis depends on a well-defined sequence of events starting with the regionalized expression of developmental patterning genes that trigger downstream mechanical forces to drive tissue remodeling at a pre-defined position. Mechanical forces can refine this genetic information by a feedback loop, however the direct implication of mechanical forces in morphogenesis robustness has never been reported.

Here, we show that a bias in force propagation ensures stereotyped morphogenesis in a mechanically noisy environment.

We found that knockdown of the Arp2/3 complex member Arpc5 specifically affects fold directionality without altering the developmental or the force patterns. By combining *in silico* modeling, biophysical and ad hoc genetic tools, our data reveal that Myosin II planar polarity

favors long-range transmission of forces and avoid force scattering, thus ensuring folding robustness by isolating the fold domain from surrounding mechanical perturbations.

Introduction

A fundamental aim in developmental biology is to unravel the mechanisms responsible for the high level of precision observed in terms of growth, scaling and patterning of tissue and organs. Morphogenesis robustness is characterized by a low level of variation of a given phenotype when given variations, such as environmental or genetic variations, occur {Félix et al., 2015; Lander, 2011}. The development of anatomical structures, even the simplest three-dimensional structures, is initiated by the establishment of precise patterning (Félix and Barkoulas, 2015; Lander, 2011). Typical illustrations of patterning-driven morphogenetic events are the differentiation of specific body structures by Hox genes (McGinnis and Krumlauf, 1992), the invagination of the mesoderm governed by the expression of Twist and Snail in Drosophila (Leptin, 1991) and somite differentiation driven by the Notch pathway in chicken (Sato et al., 2002). Patterning further induces transcriptional regulation of downstream effector molecules such as cytoskeleton regulators. The coordination of these cellular executioners creates mechanical forces that drive specific cellular behaviors and shapes (Smith et al., 2018). In turn, these mechanical forces are able to feedback on patterning regulators to refine this genetic information. Studies on morphogenesis robustness highlight the importance of functional redundancy of genes and regulatory mechanisms (Frankel et al., 2010; Smith et al., 2018), or even cytoskeletal networks (Yevick et al., 2019). However, whether mechanical forces can be directly involved in morphogenesis robustness is still an open question.

Drosophila leg development is particularly appropriate to tackle the question of morphogenesis robustness since it undergoes stereotyped morphogenesis with four strictly parallel folds formed during development (FigS1a). These folds result from the sequential activation of the Notch pathway (de Celis et al., 1998; Rauskolb and Irvine, 1999) and expression of pro-apoptotic genes (Manjón et al., 2007), each restricted to a few rows of cells in the distal part of each segment. This positional information is then translated into a “patchy” pattern of apoptotic cells in the predicted fold domain. Before their elimination, these apoptotic cells exert apico-basal forces, which constitute the initiator mechanical signals for tissue remodelling. These forces are transmitted to their neighbours

leading to an increase in apical myosin accumulation, apical constriction and eventually tissue folding (FigS1b) (Monier et al., 2015).

Results

We recently performed an unbiased screen expressing a library of RNAi in the tarsal domain of the leg (manuscript in preparation) and observed deviated folds. This phenotype was found for several components of the Arp2/3 complex known to regulate the branched actin network (Chesarone and Goode, 2009; Pollard and Beltzner, 2002; Robinson et al., 2001), including Arpc5, Arpc3a, Arpc4 and Arp2. Interestingly, defects show a wide range of variability and ranged from a complete absence of folds to fold deviation to normal folding (Fig1a). Of note, mis-oriented folds deviated from the predicted fold domain either proximally, distally, laterally or dorsally, and show different degrees of deviation (see quantification in Fig1b). This highly variable phenotype highlights a failure of morphogenesis robustness.

Since these proteins are all part of the core Arp2/3 complex and give similar phenotypes (FigS2a-b), we focused our analysis on one of them, Arpc5. Importantly, in the Arpc5 knockdown context, we found no difference at the level of Notch activation (Fig1c), apoptotic pattern formation (FigS3a-b) or ability of dying cells to generate mechanical signals compared to the control (Fig1d-e). Strikingly, our results suggest the existence of an unsuspected process constraining morphogenesis variability on top of patterning genes regulation (Fig1f). This prompted us to revisit the prevailing model of morphogenesis robustness relying on strict regulation of morphogen gradients or key identity genes (Gilmour et al., 2017).

We next asked if in the Arpc5 knockdown folds deviated towards particular regions of the tissue. During normal development, fold formation starts ventrally, progresses laterally and ends in the most dorsal region of the leg disc (Monier et al., 2015). In the Arpc5 knockdown, we noticed that folds were initiated in the correct location as shown by the regular ventral positioning of the indentations (FigS4). However, they deviated proximally or distally when reaching the lateral or dorsal region. We noticed that proximally deviated folds joined a straight cellular alignment at the distal Notch activation

border (Fig2a, FigS5a) while distally deviated folds frequently headed towards apico-basal structures of Myosin II (Fig2c) non-associated with apoptosis (FigS5b), located at various distances from the predicted fold domain. Importantly, both regions are strongly enriched in Myosin II, which usually coincides with higher tension. Laser ablation experiments showed that tension was indeed significantly higher at the "Notch border" and at non-apoptotic apico-basal myosin structures (Fig2b, d), compared to the neighboring tissue. Altogether, these data indicate that deviated folds head towards regions of high tension in absence of Arpc5 function. We hypothesized that the potential mechanical interference associated with proximal or distal structures could either be ectopically created or increased following Arpc5 knockdown, or, alternatively, present yet masked during normal development. To discriminate between these possibilities, we analyzed the Myosin II pattern in control flies. Interestingly, both the "Notch border" and non-apoptotic apico-basal myosin structures were present in the control (Fig2a, C, FigS5) and the tension borne by these structures was comparable to that measured in the Arpc5 knockdown (Fig2b,d). Altogether, these data suggest that morphogenesis is permanently challenged by surrounding remodeling events and becomes more sensitive to mechanical perturbations in the Arpc5 knockdown (see scheme in Fig2f).

To test the impact of mechanical perturbations on fold formation, we turned to *in silico* modelling. We previously developed a vertex model able to reproduce leg fold formation both in terms of tissue shape and cellular organization (Monier et al., 2015). However, this morphogenetic event was considered as an isolated process in these simulations, and the only mechanical forces applied were those originating from the apoptotic cells located in the predicted fold domain. Therefore, we implemented the model and integrated mechanical perturbations in close vicinity to the predicted fold domain, mimicking what was observed *in vivo* (see M&M, Fig2e, left panel and FigS6). Interestingly, we found that, while fold formation appeared robust in absence of potential interferences, fold shape and directionality were easily altered by local mechanical perturbation at the vicinity of the predicted fold domain (Fig2e, right panels).

105 Altogether, these results strongly suggest that some kind of isolation is required between the
106 fold domain and the neighboring tissue to avoid surrounding mechanical interference and ensure
107 morphogenesis robustness.

108 We next asked how the predicted fold domain could become insensitive to nearby mechanical
109 noise. Strikingly, in the control we noticed that Myosin II bore a polarized apical distribution within
110 the whole leg disc, with a stronger accumulation in the cellular junctions parallel to the future folds (or
111 circumferential junctions) than in perpendicular ones (or proximo-distal junctions) (Fig3a, b).
112 Consistently, Myosin II planar polarity coincided with tension anisotropy at the junction level, with
113 circumferential junctions bearing more tension than proximo-distal junctions (FigS7a-b). Importantly,
114 while the total amount of Myosin was unchanged in *Arpc5* mutants (FigS7c), Myosin II planar polarity
115 and anisotropic junctional tension were lost in *Arpc5* knockdown (Fig3a-b and FigS7b). These
116 observations show that folding robustness is associated with planar polarization of Myosin II in the fly
117 leg.

118 We then asked how Myosin II polarity could protect morphogenesis from surrounding
119 mechanical disturbances, ensuring robust fold formation.

120 Fold formation relies upon the transmission of apoptotic forces to the apical surface of
121 neighboring living cells that stretch, constrict and ultimately create the fold (Monier 2015). We
122 therefore hypothesized that Myosin II polarized distribution could generate a bias in long-range force
123 transmission, favoring the transmission of apoptotic forces in the direction of the future fold and
124 avoiding force scattering across the tissue. To test this hypothesis, we compared force transmission in
125 the presence or in the absence of Myosin II planar polarity. Potential bias in force propagation was
126 visualized by analysing the tension pattern in close vicinity to a local mechanical force, compare to the
127 basic tension pattern of the tissue. We first analyzed the basic tension pattern at the multicellular level
128 by performing circular cutting. In the control, circular cutting induced an ovoid-shaped recoil (Fig3c),
129 indicating that tissue tension was stronger in the circumferential axis. The same experiment performed
130 in the *Arpc5* knockdown resulted in a circular recoil, indicating that basic tension anisotropy was lost
131 (Fig3c). To specifically analyze force transmission at the apical surface of the leg epithelium, we next

132 generated ectopic forces by laser ablation-induced wound healing (Fernandez-Gonzalez and Zallen,
133 2013). To do so, we first wound the tissue locally at the level of a tricellular junction, waited for the
134 tissue to repair, and as soon as the healing started generating local forces, we performed a circular cut
135 around the healing region and observed the recoil (Fig3d). Then, in order to specifically analyze force
136 transmission, we compared this release with that observed in absence of preliminary local wound
137 healing. By this way, we observed that in the control, forces generated locally and in a controlled
138 manner are transmitted preferentially in the circumferential direction (the dark grey region in Fig3e is
139 more important for 90° than for 0°). However, this is no longer the case when Myosin polarity is lost
140 following Arpc5 knockdown (the dark blue region in Fig3e is similar irrespective of the angle). We
141 conclude that Arp2/3 controls junctional tension anisotropy through Myosin II planar polarity to avoid
142 apical force scattering, leading to biased force transmission along the circumferential axis during leg
143 development.

144 To directly test the impact of Myosin II planar polarity on fold robustness *in vivo*, we disrupted
145 Myosin II polarity by an independent method. We generated a new variant of the nanobody-based
146 GFP-trap technique previously described (Harmansa et al., 2017; Harmansa et al., 2015), and made
147 Myosin II distribution isotropic by trapping a Myosin II::GFP fusion protein (Myosin Regulatory
148 Light Chain, MRLC::GFP) at the adherens junction (Fig4a-b, FigS8, see M&M). Interestingly, using
149 conditional expression of this Ajs-GFP-trap construct in the presence of Myosin::GFP, we frequently
150 observed deviated folds, mimicking the defects observed in the Arpc5 knockdown (Fig4c, compare to
151 Fig1a), while expression of AJs-GFP-trap in absence of any GFP does not alter leg morphognesis
152 (FigS8b). These experiments show that decreasing or abolishing Myosin II planar polarity through two
153 independent strategies (Arpc5 loss-of-function and artificially forced Myosin II-GFP isotropic
154 redistribution) leads to deviated folds in the fly leg.

155 We therefore wondered whether restoring Myosin II polarity in a non-polarized tissue could
156 rescue the defects of fold deviation. Although not feasible *in vivo*, we addressed this question using *in*
157 *silico* modelling, asking whether fold deviation caused by local mechanical perturbations (Fig2e)
158 could be rescued by the introduction of planar polarized junctional tension. For this, we mimicked

Myosin II planar polarity and the associated tension anisotropy by the attribution of different values of junctional tension depending on junction orientation (see M&M and FigS9). Interestingly, gradual increase of tissue polarity favors fold straightness and insensitivity to surrounding perturbations (Fig4d). Altogether, *in vivo* manipulations and *in silico* modelling indicate that the planar polarization of tissue tension favors mechanical isolation of fold formation, which ultimately increases morphogenesis robustness.

Discussion

Altogether, this work reveals the existence of a new mechanism ensuring morphogenesis robustness, on top of developmental patterning, through the channeling of mechanical forces (Fig4e). It highlights a new role for Myosin II planar polarity in long-range force propagation, which isolates mechanically morphogenesis from potential nearby interferences.

This work further reveals that fold morphogenesis in the Drosophila developing leg occurs in the presence of mechanical noises, which is most probably a general feature of morphogenetic events. Thus, it is tempting to speculate that mechanical isolation could be required in a wide variety of morphogenetic processes to avoid force scattering and maintain morphogenesis robustness.

178

179 **References**

180 Anlaş, A.A., and Nelson, C.M. (2018). Tissue mechanics regulates form, function, and dysfunction.
181 Curr Opin Cell Biol *54*, 98-105.
182 Bertet, C., Sulak, L., and Lecuit, T. (2004). Myosin-dependent junction remodelling controls planar cell
183 intercalation and axis elongation. Nature *429*, 667-671.
184 Blankenship, J.T., Backovic, S.T., Sanny, J.S., Weitz, O., and Zallen, J.A. (2006). Multicellular rosette
185 formation links planar cell polarity to tissue morphogenesis. Dev Cell *11*, 459-470.
186 Chesarone, M.A., and Goode, B.L. (2009). Actin nucleation and elongation factors: mechanisms and
187 interplay. Curr Opin Cell Biol *21*, 28-37.
188 de Celis, J.F., Tyler, D.M., de Celis, J., and Bray, S.J. (1998). Notch signalling mediates segmentation of
189 the Drosophila leg. Development *125*, 4617-4626.
190 Fernandez-Gonzalez, R., and Zallen, J.A. (2013). Wounded cells drive rapid epidermal repair in the
191 early Drosophila embryo. Mol Biol Cell *24*, 3227-3237.
192 Frankel, N., Davis, G.K., Vargas, D., Wang, S., Payre, F., and Stern, D.L. (2010). Phenotypic robustness
193 conferred by apparently redundant transcriptional enhancers. Nature *466*, 490-493.
194 Félix, M.A., and Barkoulas, M. (2015). Pervasive robustness in biological systems. Nat Rev Genet *16*,
195 483-496.
196 Harmansa, S., Alborelli, I., Bieli, D., Caussinus, E., and Affolter, M. (2017). A nanobody-based toolset
197 to investigate the role of protein localization and dispersal in. Elife 6.
198 Harmansa, S., Hamaratoglu, F., Affolter, M., and Caussinus, E. (2015). Dpp spreading is required for
199 medial but not for lateral wing disc growth. Nature 527, 317-322.
200 Gilmour, D., Rembold, M., and Leptin, M. (2017). From morphogen to morphogenesis and back.
201 Nature *541*, 311-320.
202 Lander, A.D. (2011). Pattern, growth, and control. Cell *144*, 955-969.
203 Lecuit, T., Lenne, P.F., and Munro, E. (2011). Force generation, transmission, and integration during
204 cell and tissue morphogenesis. Annu Rev Cell Dev Biol *27*, 157-184.
205 Leptin, M. (1991). twist and snail as positive and negative regulators during Drosophila mesoderm
206 development. Genes Dev *5*, 1568-1576.
207 Manjón, C., Sánchez-Herrero, E., and Suzanne, M. (2007). Sharp boundaries of Dpp signalling trigger
208 local cell death required for Drosophila leg morphogenesis. Nat Cell Biol *9*, 57-63.
209 McGinnis, W., and Krumlauf, R. (1992). Homeobox genes and axial patterning. Cell *68*, 283-302.
210 Monier, B., Gettings, M., Gay, G., Mangeat, T., Schott, S., Guarner, A., and Suzanne, M. (2015). Apico-
211 basal forces exerted by apoptotic cells drive epithelium folding. Nature *518*, 245-248.
212 Pollard, T.D., and Beltzner, C.C. (2002). Structure and function of the Arp2/3 complex. Curr Opin
213 Struct Biol *12*, 768-774.
214 Rauskolb, C., and Irvine, K.D. (1999). Notch-mediated segmentation and growth control of the
215 Drosophila leg. Dev Biol *210*, 339-350.
216 Robinson, R.C., Turbedsky, K., Kaiser, D.A., Marchand, J.B., Higgs, H.N., Choe, S., and Pollard, T.D.
217 (2001). Crystal structure of Arp2/3 complex. Science *294*, 1679-1684.
218 Sato, Y., Yasuda, K., and Takahashi, Y. (2002). Morphological boundary forms by a novel inductive
219 event mediated by Lunatic fringe and Notch during somitic segmentation. Development *129*, 3633-
220 3644.
221 Smith, S.J., Rebeiz, M., and Davidson, L. (2018). From pattern to process: studies at the interface of
222 gene regulatory networks, morphogenesis, and evolution. Curr Opin Genet Dev *51*, 103-110.
223 Spitz, F., and Furlong, E.E. (2012). Transcription factors: from enhancer binding to developmental
224 control. Nat Rev Genet *13*, 613-626.

Urbano, J.M., Naylor, H.W., Scarpa, E., Muresan, L., and Sanson, B. (2018). Suppression of epithelial folding at actomyosin-enriched compartment boundaries downstream of Wingless signalling in. Development *145*.
Yevick, H.G., Miller, P.W., Dunkel, J., and Martin, A.C. (2019). Structural Redundancy in Supracellular Actomyosin Networks Enables Robust Tissue Folding. Dev Cell *50*, 586-598.e583.

Acknowledgements

We thank Michel Labouesse and Yohanns Bellaiche for their constructive comments on the manuscript. MS's lab is supported by grants from the European Research Council (ERC) under the European Union Horizon 2020 research and innovation program (grant number EPAF: 648001), and from the Institut National de la Santé et de la Recherche Médicale (Inserm, Plan cancer 2014-2019). EM has a post doc fellowship from the Association pour la Recherche contre le Cancer (ARC).

Author contributions

EM conceived and performed the experiments in fly leg discs. ST participated in modelling conception and realized all the simulations. EM and ST analysed and quantified the data**.** BM participated in experimental conception and article writing. GG supervised the modelling conception. MS supervised the project, wrote the paper and provided the funding.

Competing interest declaration

The authors declare no competing financial interests.

Corresponding authors

Correspondence and requests should be addressed to M.S. (magali.suzanne@univ-tlse3.fr) for biology and materials and to G.G. (guillaume@morphogenie.fr) for modelling.

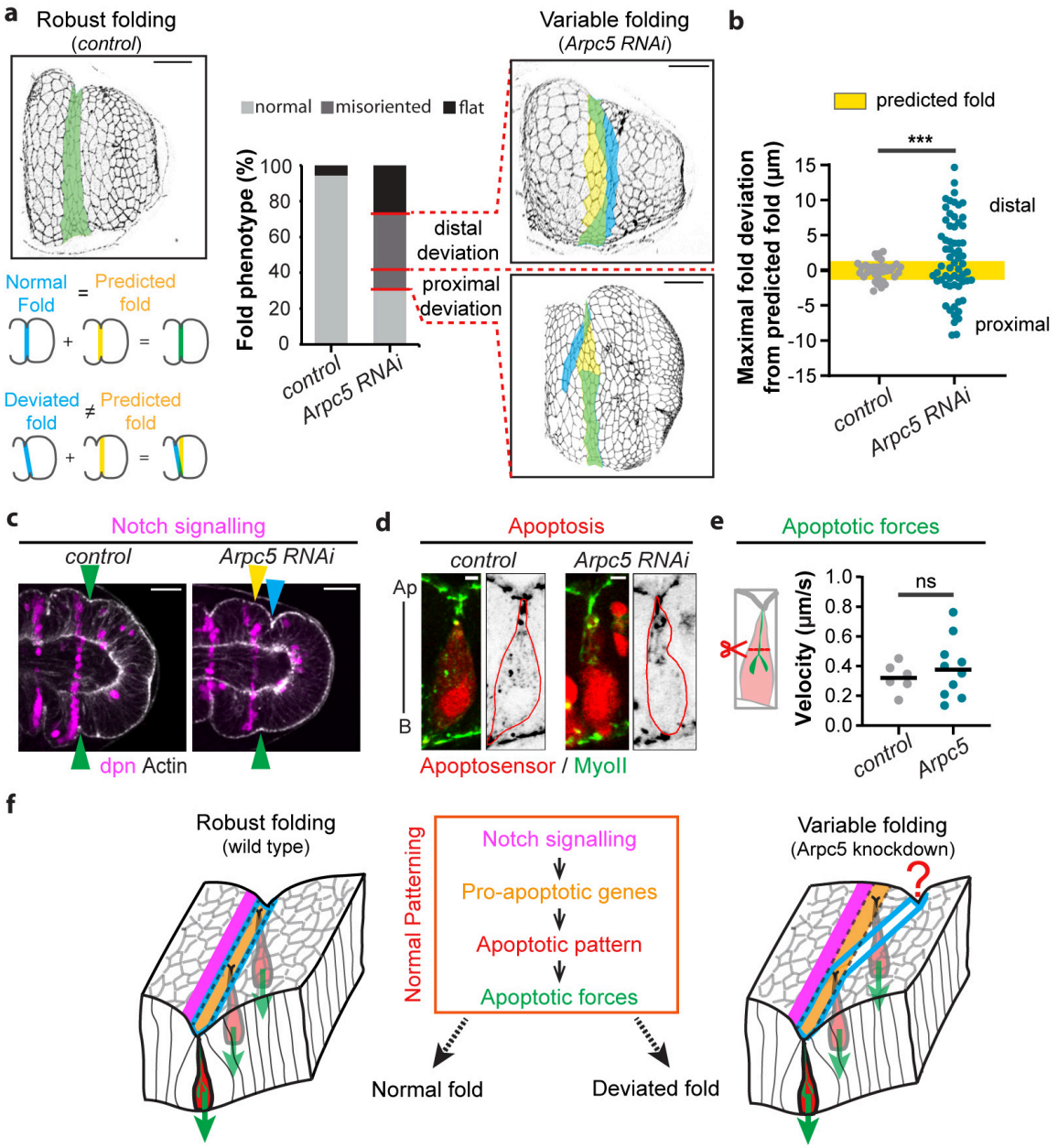

Figure 1: Morphogenesis variability in Arpc5 knockdown**.**

a, Fold morphology in *control* or *Arpc5* RNAi animals expressing β-catenin::GFP (*arm::GFP*). Predicted fold is highlighted in yellow, real fold in blue and perfect match between them in green. Note the variability of the phenotype observed in *Arpc5* RNAi as shown by deviation either proximal or distal to the predicted fold domain. The histogram shows the repartition of phenotypes of the distal-most fold in *control* and *Arpc5* RNAi (n=54, 60 legs, respectively). **b**, Dot plot showing the maximal distance of the real fold from the predicted fold (highlighted in yellow) in control (*sqh::RFPt[3B]; Dll-Gal4, UAS-GC3Ai*) and Arpc5 RNAi (*sqh::RFPt[3B]; Dll-Gal4, UAS-GC3Ai; UAS Arpc5RNAi*) (n=35, 63 legs, respectively). A *F*-test of equality of variances has been calculated to compare the variability of the phenotype. ***, p-value < 0.001. **c,** Single plane confocal images of *control* or *Arpc5* RNAi legs stained with phalloidin (white) and showing Z-projection of anti-deadpan (magenta). Yellow, blue and green

264 arrowheads indicate predicted fold, real fold and perfect match between them respectively. **d,**
265 Sagittal views showing apoptotic myosin cables in *control* (*sqh::RFPt[3B]; Dll-Gal4, UAS::GC3Ai*) and
266 *Arpc5* RNAi (*sqh::RFPt[3B]; Dll-Gal4, UAS::GC3Ai; UAS::Arpc5RNAi*). **e,** Dot plot showing the initial
267 velocity of apoptotic cable recoil after laser microdissection in *control* (*sqh::GFP[29B]; Dll-Gal4*) and
268 *Arpc5* RNAi (*sqh::GFP[29B]; Dll-Gal4; UAS::Arpc5RNAi*) (n=6 and 10, respectively). Black line indicates
269 the median. Statistical significance has been calculated using Mann-Whitney U test. ns, not
270 significant. **f,** Schematics of folding observed in *control* or *Arpc5 RNAi*. Scale bar represents 20 µm in
271 **a**, **c**, and 2 µm in **d**.

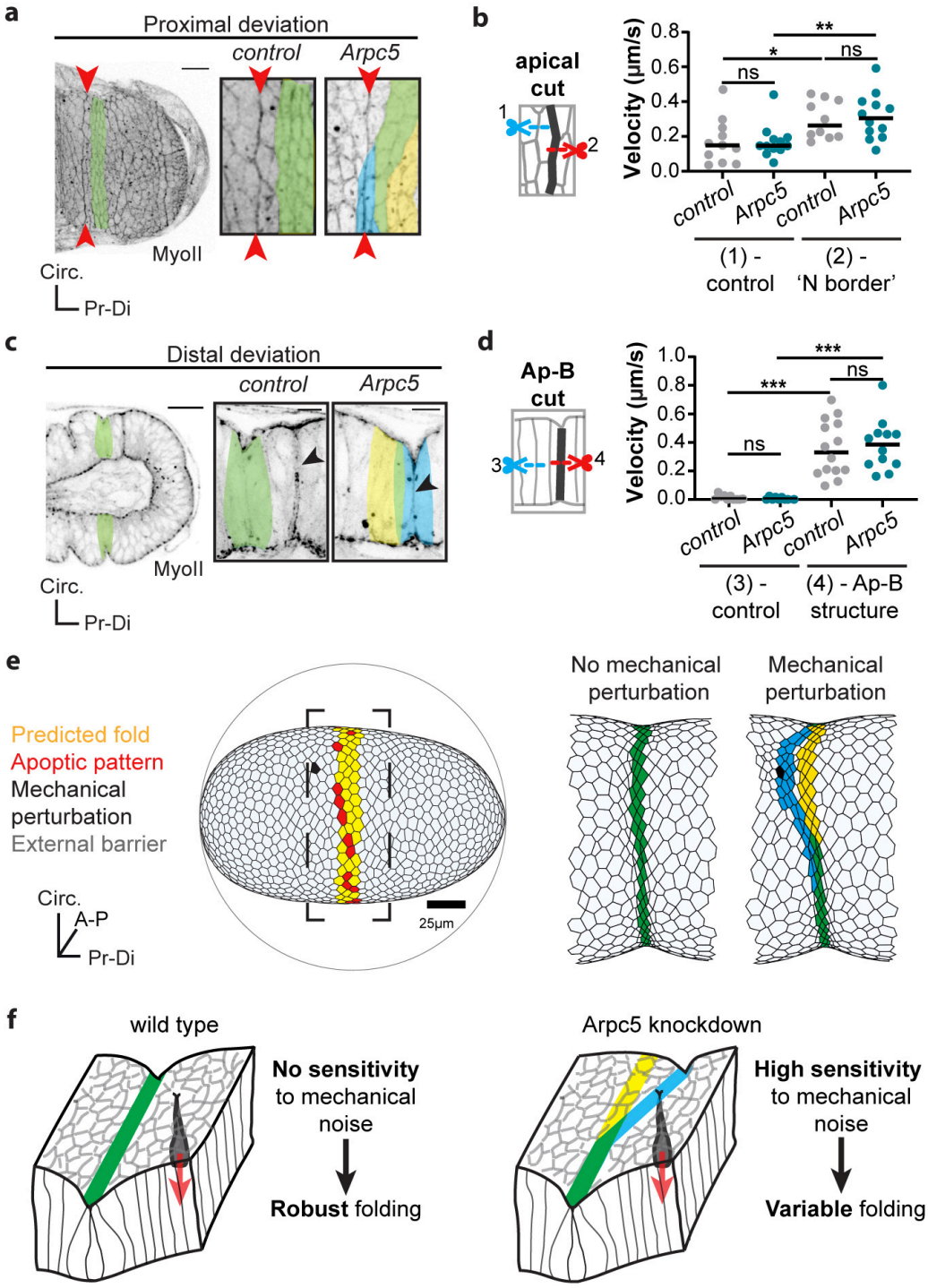

Figure 2: Morphogenesis occurs in a mechanically noisy environment.

a, MRLC::GFP (*sqh::GFP[29B]*) leg disc showing the 'Notch border' (between red arrowheads) in *control* (*sqh::GFP[29B]; Dll-Gal4*) and *Arpc5* RNAi (*sqh::GFP[29B]; Dll-Gal4; UAS::Arpc5RNAi*) legs. **b,** Dot plot of the initial recoil velocity observed after microdissection of adherens junctions at the 'Notch border' or adjacent junctions in *control* (*sqh::RFPt[3B]; Dll-Gal4; arm::GFP*) and *Arpc5* RNAi (*sqh::RFPt[3B]; Dll-Gal4; arm::GFP, UAS::Arpc5RNAi*) (n=11, 12, 10 and 12 respectively). **c,** Confocal images showing non-apoptotic apico-basal myosin structure (black arrowhead) in *control* (*sqh::GFP[29B]; Dll-Gal4*) and *Arpc5* RNAi (*sqh::GFP[29B]; Dll-Gal4; UAS::Arpc5RNAi*). **d,** Dot plot of

the initial recoil velocity of non-apoptotic apico-basal myosin structure or lateral membrane after laser dissection in *control* (*sqh::GFP[29B]; Dll-Gal4*) and *Arpc5* RNAi (*sqh::GFP[29B]; Dll-Gal4; UAS::Arpc5RNAi*) (n=14, 12, 10 and 10 respectively). **e,** (Left) General view of the virtual tissue. Cells from the predicted fold domain are indicated in yellow, apoptotic cells in red. The tissue is constrained by a spherical external barrier represented by the grey circle. The black dotted square corresponds to the close-up shown on the right**.** (Right) Simulations showing lateral views of maximal fold depth with or without mechanical perturbation (indicated in black). **f,** Schematics of folding in wild type or Arpc5 knockdown contexts in presence of mechanical noise (red arrow). In **a**, **c**, **e** and **f**, predicted fold is highlighted in yellow, real fold in blue and perfect match between them in green. In **b, d**, black lines indicate the median. Statistical significance has been calculated using Mann-Whitney U test. ns, not significant; *, p-value < 0.05; **, p-value < 0.01; ***, p-value < 0.001. Scale bar represents 20 µm in **a** and **c**.

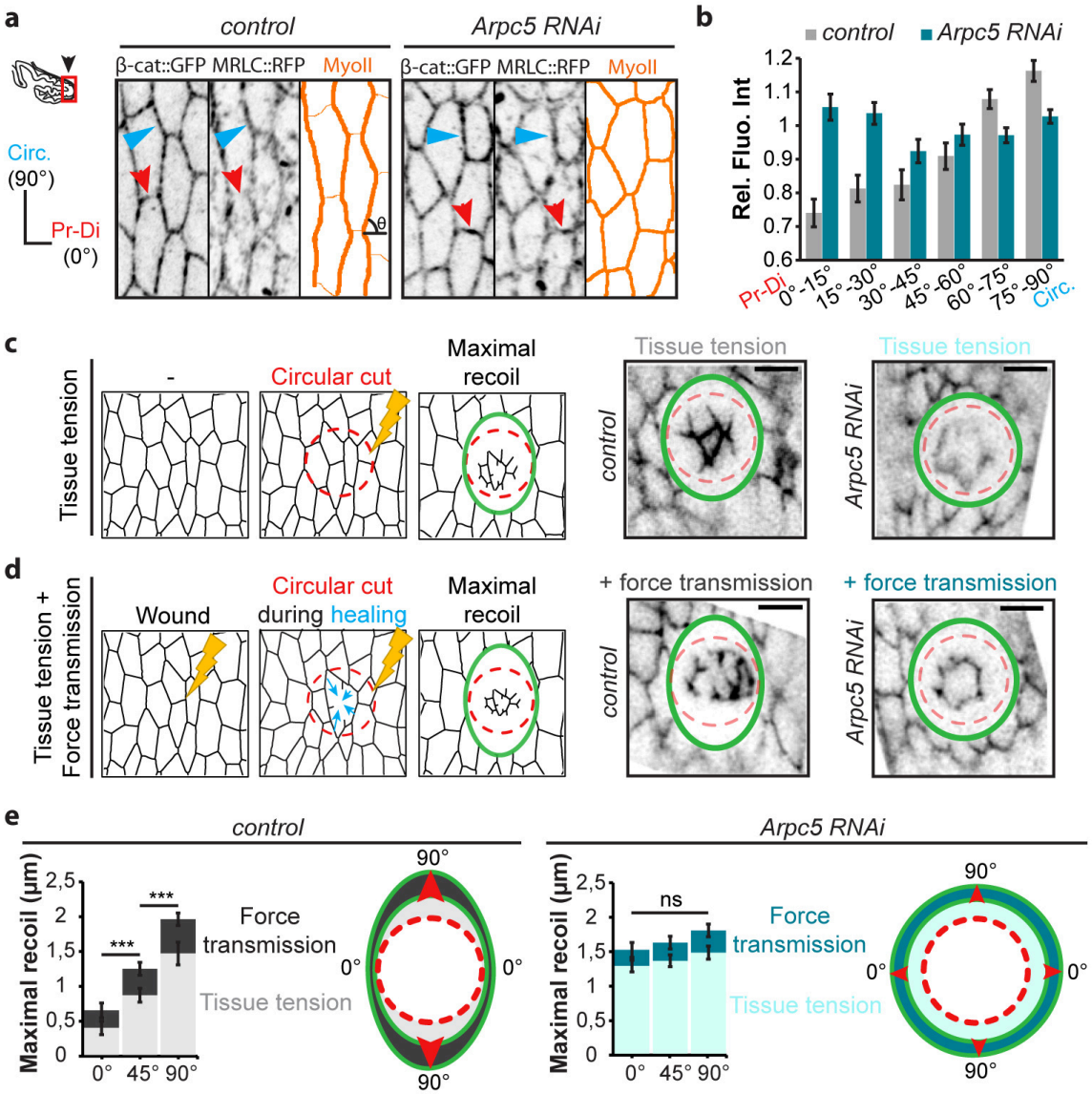

293

294 **Figure3: Planar polarity favors directional force transmission.**

295 **a,** Confocal images showing the distribution of β-catenin::GFP and myosin II (*sqh::RFPt[3B]*) in
296 *control* and *Arpc5* RNAi. Red and blue arrowheads respectively indicate proximo-distal and
297 circumferential junctions. Myosin II junctional distribution is schematized in orange. **b,** Quantification
298 of the myosin distribution at junction in *control* and *Arpc5* RNAi (n= 621 and n= 972 junctions
299 respectively). **c-d,** Maximal recoil after circular ablation corresponding to global tissue tension (**c**, no
300 wound healing) or global tissue tension and additional force transmission (wound healing, **d**) in
301 *control* (*Dll-Gal4; arm::GFP*) and *Arpc5* RNAi (*Dll-Gal4; arm::GFP, UAS::Arpc5RNAi*). Maximal recoil of
302 the tissue and initial positioning of the circular ablation are indicated by the green and dashed red
303 lines respectively. **e,** Quantification of the maximal recoil of the tissue in absence (light grey and light
304 blue) or presence (dark grey and dark blue) of wound in *control* and *Arpc5* RNAi (n= 10, 10, 12, 10
305 respectively). Schemes on the right highlight the pattern of force transmission (dark colors). In **e,**
306 statistical significance has been calculated using Mann-Whitney U test. ns, not significant; *** p-
307 value < 0, 001. Graph bars in **b** and **e** correspond to the mean ± SEM. Scale bar represents 5 µm in **a**,
308 **c** and **d**.

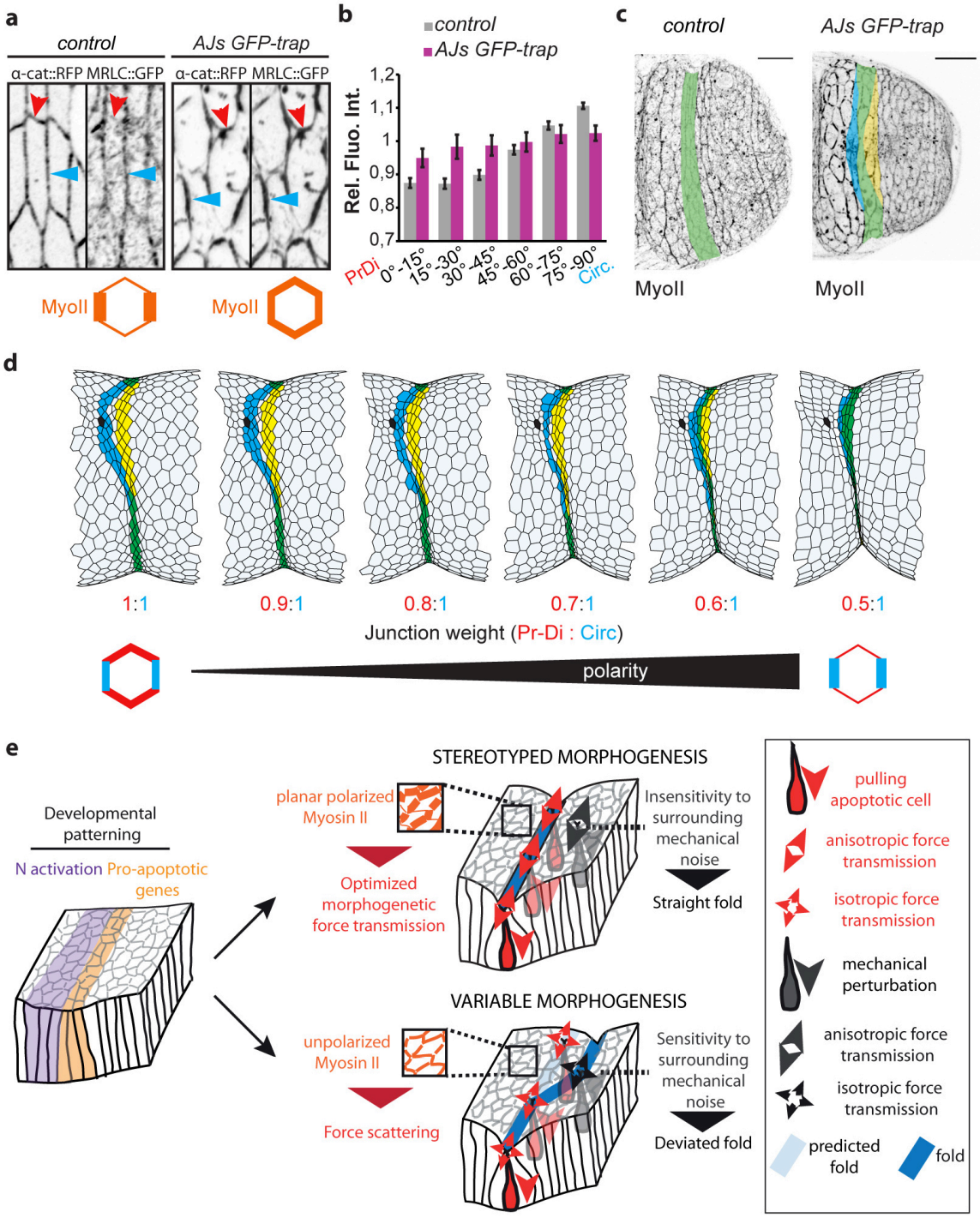

Figure 4: Planar polarity ensures morphogenesis robustness.

a, Close up views of confocal images showing the distribution of myosin II in control (*sqh::GFP[29B]; ap-Gal4, UAS α-catenin::TagRFP)* or *AJs GFP-trap* (*sqh::GFP[29B]; tubG80ts; ap-Gal4, UAS vhhGFP4::α-catenin::TagRFP*). Red and blue arrowheads respectively indicate proximo-distal and circumferential junctions. Myosin distribution is schematized in orange. **b,** Quantification of Myosin II distribution in the absence (*sqh::GFP[29B]; ap-Gal4, UAS α-catenin::TagRFP*) or in presence of the AJs-GFP-trap construct (*sqh::GFP[29B]; tubG80ts; ap-Gal4, UAS vhhGFP4::α-catenin::TagRFP*). (n= 2063 and n= 736 junctions respectively). **c,** Confocal images of the leg distal-most fold in presence or

absence of the AJs-GFP-trap construct (same genotypes as in **a, b**) showing fold deviation in absence of Myosin II polarity. Deviation of fold represents 0/15 and 8/12, respectively for control and AJs-GFP-trap. Predicted fold domain is highlighted in yellow, real fold in blue and perfect match between them in green. Scale bar represents 20 µm. **d,** Lateral views of simulations including mechanical perturbation (in black) for different values of junction weight ratio (i.e. tension anisotropy). Predicted fold domain is highlighted in yellow, real fold in blue and perfect match between them in green. **e**, Schematics of tissue folding with or without tissue planar polarity. Note that Myosin II planar polarity drives anisotropic force transmission, thus isolating mechanically the morphogenesis of the fold, while in absence of Myosin II planar polarity, forces are scattered in the tissue, making fold formation more variable and sensitive to nearby mechanical perturbation.

Supplementary Materials
Materials and Methods
Table S1
Fig S1 – S9
References (26 – 31)

Materials and Methods

Fly stocks and genetics

Dll^{EM212}::Gal4, ap^{md544}::Gal4, hh::Gal4, arm::arm::GFP were obtained from Bloomington Drosophila Stock Center (BDSC). sqh::eGFP^{KI}[29B], sqh::RFPt^{KI}[3B] and the GFP apoptosensor UAS::GC3Ai were described previously (Ambrosini et al., 2019; Schott et al., 2017). ap^{42B11}::Gal4 and UAS::α-catenin::TagRFP are gift from C. Estella and K. Sugimura.

RNAi experiments were realized using UAS::Arpc3A-RNAi (JF02370), UAS::Arpc5-RNAi (JF03147), UAS-Arp2 RNAi (JF02785), UAS-lacZ, obtained from BDSC.

Generation of transgenic flies

To trap Myosin::GFP at junctions, we constructed a p*UASt–vhhGFP4-α-catenin::TagRFP* (AJs GFP-trap). To do so, *α-catenin::TagRFP* was amplified by PCR with specific primers from a pUAS-Dαcatenin-TagRFP (kindly provided by Dr K. Sugimura). vhhGFP4 was amplified by PCR from nanoGFP-cry2 plasmid (gift from Dr Le Borgne). A 36nt sequence was added in the reverse primer to create a GSAGSAAGSGEF linker between the GFP-trap sequence and α-catenin::TagRFP sequence. These two fragments were successively cloned using InFusion technology in pUASt-attB plasmid cut with KpnI.

The resulting p*UASt–vhhGFP4-α-catenin::TagRFP* plasmid was injected into flies carrying attP2 landing sites on the third chromosome to produce transgenic flies.

Immunostaining

Imaginal leg discs were dissected after 48h at 29°C at prepupal stage (1.5 hours after pupae formation – APF) in PBS 1X. Imaginal discs were fixed 20' in paraformaldehyde 4% diluted in PBS 1X., then washed in PBS 1X and either mounted in Vectashield (Vectors laboratories) or extensively washed in PBS-Triton 0.3%-BSA 1% (BBT) and incubated overnight at 4°C with appropriate dilutions of primary antibodies in BBT. Rat anti-deadpan antibody (Abcam – ab195172) was used at 1:100 dilution, rabbit anti-dcp1 (Cell Signaling Technology – 9578S) at 1:200, and chicken β-galactosidase (GeneTex – GTX77365) at 1:1000. After washes in BBT, imaginal leg discs were incubated at room temperature for 2 h with 1:200 anti-rat IgG 647, anti-rat IgG 555, anti-rabbit IgG 555 or anti-chicken IgG 488 (obtained from Interchim) with or without phalloidin (Alexa488 at 1:500 or rhodamin at 1:500 – Fisher Scientific). Then, samples were washed in PBS-Triton 0.3%, suspended in Vectashield (Vectors laboratories) and mounted on slides.

Confocal imaging

Samples were analyzed using a LSM880 confocal microscope which included a Fast Airyscan module (Carl Zeiss) and is equipped with a Plan-Apochromat 40x/NA 1.3 Oil DIC UV-IR M27 objective. Z-stack were acquired using either the classical confocal mode or the High Resolution mode (Airyscan) was used with a pixel size of 0.046 µm/pixel and a *z*-step of 0.220 um. Airyscan Z-stacks were processed b in ZEN software using the automatic strength (6 by default) and the 3D method.

Ex vivo culture of leg imaginal disc

Imaginal leg discs were dissected from prepupal stage (1.5 hours APF at 29°C) in Schneider's insect medium (Sigma-Aldrich) supplemented with 15 % fetal calf serum and 0.5 % penicillin-streptomycin as well as 20-hydroxyecdysone at 2 µg/mL (Sigma-Aldrich, H5142). Leg discs were transferred on a slide in 12 µL of this medium in a well formed by a 120 µm-deep double-sided adhesive spacer (Secure-SealTM from Sigma-Aldrich). A coverslip was then placed on top of the spacer. Halocarbon oil was added on the sides of the spacer to prevent dehydration.

Image analysis

Quantification of the fold variability

We characterize the variability of fold formation for legs displaying normal or deviated folds, in the *control* and in *Arpc5 RNAi*. Basically, the distance between the Notch signaling – labelled by deadpan immunostaining – and the fold was measured using the straight line tool in ImageJ. The measure corresponds to the maximal distance between the fold and the deadpan staining. To calculate the real deviation from the predicted fold domain, we substract the mean distance obtained for control legs to each value. Standard deviation of control legs was measured and used to define predicted fold (± 1.30 µm from the mean), which is highlighted in yellow on the graph in Figure 1b.

Measurement of the planar polarity

Using the surface tool on Imaris (Bitplane), a mask was created from the junctional labelling (arm::GFP or α-catenin::RFP) to quantify the Myosin II present at junctions. From this new Z-stack, the maximum of intensity (MaxProj) and the sum of intensity (SumProj) were projected using Fiji (ImageJ 1.51s – NIH). Then, from the MaxProj, a skeleton was created and each junction were individualized by suppressing nodes. This template was used to identify each junction as a region of interest (ROI). From these ROIs, the angle – in relation to the proximal-distal axis – and the raw fluorescence intensity of each junction were measured on the SumProj. A visual control was then performed and a manual correction done if required.

The junctional mean of fluorescence intensity was normalized to the global junctional mean

$$I_{Rj} = \frac{\overline{I_j}}{1 \quad \overline{}}$$

of fluorescence intensity in the corresponding leg domain.

Quantification of the apical myosin

Using ImageJ software, a segmented line was drawn along the apical surface in hedgehog and control domain on five different slices for each leg acquired. For each slice, the mean of fluorescence intensity was measured and the ratio between hedgehog domain and control

domain was calculated. The mean of these five ratios per leg is represented as one spot on the graph in Supplemental Figure 7.

Laser ablation

Laser ablation experiments were performed using a pulsed DPSS laser (532 nm, pulse length 1.5 ns, repetition rate up to 1 kHz, 3.5 µJ/pulse) steered by a galvanometer-based laser scanning device (DPSS-532 and UGA-42, from Rapp OptoElectronic, Hamburg, Germany) and mounted on a LSM880 confocal microscope (Carl Zeiss) equipped with a 63x C-Apochromat NA 1.2 Water Corr objective (Carl Zeiss). Photo-ablation of apical junction was done in the focal plane by illuminating at 70 % laser power during 1 s. This focal plane was acquired every 0.551 s, during 10 s before and at least 45 s after ablation, with a pixel size of 0.13 µm/pixel. Photo-ablation of apico-basal Myosin II enrichment was done in the focal plane by illuminating at 100 % laser power during 2-2.5 s along a 45-50 pixel line. This focal plane was acquired every 0.551 s, during 5 s before and at least 45 s after ablation, with a pixel size of 0.13 µm/pixel. Data analysis was performed with the ImageJ software using a home-made macro.

For circular photo-ablation, the focal plane was illuminated during 4-5 s along a 45 pixel radius circle (Figure 3c). This focal plane was acquired every 0.551 s, during 10 s before and at least 45 s after ablation, with a pixel size of 0.13 µm/pixel. For the second set of experiments (wound healing), tissue was firstly wound at the level of a tricellular junction by illuminating during 4-5 s along a 10 pixel radius circle and then ablate circularly during the healing phase using the circular shape described above (see Figure 3d). Data analysis was performed with the ImageJ software. Briefly, the distance between the location of the circular cut and the maximal recoil induced by this ablation was measured at 0° (proximo-distal axis), 45° and 90° (circular axis) using the line tool.

Modeling

Initial tissue generation

We modeled the most distal part of the leg imaginal disc [fig1-a], before the T4-T5 fold formation begins as a 2D meshwork around a cylinder caped by two hemispheres, oriented along the proximo-distal axis. We started with a mostly hexagonal lattice with a perimeter of 23 cells and a length of 15 cells. We perform two rounds of cell divisions with a random division axis to randomize the polygonal cell side number and create an approximately 50 by 30 apical junctions meshwork. Diversity of cell shapes is increased by adding variability to the cells' preferred areas, normally distributed with an 8% variance. The initial tissue has 1652 cells, is 200 µm long in its proximo-distal axis and 100 µm in diameter.

Mechanical model

The epithelium shape is given by the quasi-static equilibrium of a potential energy dependent on the junctional mesh geometry, following our previous work (Gracia et al., 2019; Monier et al., 2015).

This energy is given in equation (1) and is comprised of three cell-level terms and two constrain terms. At the cell level, apical shape is governed by area and perimeter elasticity terms, following (Bi et al., 2015). To these terms, we add a linear apico-basal tension for the apoptotic cells, dependent on cell height. Two more terms ensure maintenance of the overall tissue shape. First, the total volume of the tissue is maintained by an elastic constrain. Second, an external barrier is modeled as a sphere surrounding the tissue; when the distance of a vertex from the sphere center is higher than the sphere radius, it is pulled back to this radius by an elastic force.

$$E = \sum_{\alpha} \left(\frac{K_\alpha}{2} \left(A_\alpha - A_{\alpha,0} \right)^2 + \frac{K_p}{2} (P - P_{\alpha,0})^2 + T_\alpha^{\mathrm{ab}} h_\alpha \right) + \frac{K_V}{2} (V - V_0)^2 + \sum_i \frac{K_b}{2} \delta^+ R_i^2 \qquad (1)$$

The value of (K^V) was chosen at the lowest value such that compression of the tissue by cellular contractility and the effect of the lumen on the fold formation was minimal and kept the tissue integrity (see FigS6). Here $\sum_\alpha$ marks the sum over every polygonal cell and $\sum_i$ a sum over every vertex. Apico-basal tension is exerted from the vertices towards the proximo-distal axis. We consider an anchor point i' as the protection of the vertex i onto the proximo-distal axis. i' is rigidly fixed to this axis. The penetration depth $\delta^+ R_i$ is defined by:

$$\delta^+ R_i = \begin{cases} R_i - R_p & \text{if } R_i > R_b \\ 0 & \text{if } R_i \leq R_b \end{cases} \qquad (2)$$

Energy minimum is reached through a gradient descent strategy using the Broyden-Fletcher-Goldfarb-Shanno bound constrained minimization algorithm from the scipy library (van der Walt et al., 2011).

Tissue anisotropy

In vivo, cell polarity translates in different mechanical properties for different cell junctions. Here, in order to create the cell anisotropy (the ratio between the long axis and the perpendicular axis of the apical surface of the cell), we change the calculus of the apical perimeter by adding a weight on each cell junction. The modified perimeter is calculated as the weighted sum

$$P^* = \frac{\sum_{ij \in \alpha} \omega_{ij} l_{ij}}{\sum_{ij \in \alpha} \omega_{ij}} n_\alpha \qquad (3)$$

Where $\sum_{ij \in \alpha}$ denotes a sum over all edges of cell α and ω_{ij} is the weight of the junction ij, l_{ij} is the length of the junction ij and n_α is the number of sides of cell α. Note that this weighted sum is equal to the actual perimeter when all weights are equals, and allows to model polarity without direct modification of the other dynamical parameters.

We set two different values of the weight depending on whether the edge is in the circumferential axis ($\omega_{//}$) or in the proximo-distal axis ($\omega_\perp$). Weight is higher for circumferential edges than for proximo-distal one (Supplementary fig 9). As cell shapes are on average hexagonal, we set the boundary between parallel and perpendicular junctions at $\pi/3$.

Apoptotic process

Around 30 apoptotic cells are chosen randomly in the fold region according to a probability density described in our previous work (Monier et al., 2015). The tissue deforms progressively as apoptotic cells undergo apical constriction and apico-basal traction through gradual changes in their mechanical parameters, while other cells passively follow the deformation.

A cell starts apoptosis at time step t_i such that $t_i = t_f \frac{\phi_\alpha}{\pi}$ where ϕ_α is the angle of the cell's apical surface face center with respect to the dorso-ventral axis and t_f the final simulation time.

Apoptosis is modeled as a sequence of apical constriction and apico-basal traction.

Apical constriction consists in a reduction of the cell's preferred perimeter $P_{\alpha,0}$ at a constant rate $\sqrt{\tau_\alpha}$ and a reduction of its preferred area $A_{\alpha,0}$ at constant rate τ_α until the cell area reaches a threshold

A_c as given in equation (4). Once the critical area is reached, preferred area and preferred perimeters are maintained constant.

$$\begin{cases} P_{\alpha,0}(t) = \dfrac{P_{(\alpha,0)}(t-1)}{\sqrt{\tau_\alpha}} \\ A_{\alpha,0}(t) = \dfrac{A_{(\alpha,0)}(t-1)}{\tau_\alpha} \end{cases} \qquad if\ A_{\alpha,t} > A_c \tag{4}$$

During the apical constriction phase, contraction is propagated to neighboring cells. Contraction rate τ_β of a neighboring cell β decreases linearly as the cell is farther away from the apoptotic cell:

$$\tau_\beta = \tau_\alpha - \frac{r}{r_{\max}}(\tau_\alpha - \tau_{\min}) \tag{5}$$

Here $r = 1$ if the cell β is a direct neighbour of the apoptotic cell, 2 if it's a second order neighbor, and so on. $r_{\max}$ is the span of the propagation and τ_{min} the contraction rate for cells at r_{max} from the apoptic cell.

Each apoptotic cell can develop an apico-basal tension, during and after the constriction phase, with probability $p = \exp(-A_\alpha/A_c)$. Traction takes place for N_t time steps, during which the apico-basal tension exerted on the face is T^{ab}

Mechanical perturbation

We modeled a mechanical perturbation on the fold formation as one disrupting cell at a $r_p = 3$ cells distance from the fold position in the lateral-dorsal part of the tissue. The disrupting cell dynamic is similar to apoptotis, with apical constriction and apical-basal tension. Apical constriction starts at the beginning of the simulation, and when the critical area is reached, traction is applied until the end of the simulation. At the depth measurement, the traction is active. For every simulation, apart from the time span for which the mechanical perturbation is exerted, the parameters for the perturbing cell are identical to the parameters for the apoptotic cell.

Choice of parameter values.

The unit energy (denoted by u) is defined so that the area elasticity modulus K_α equals 1 $u/\mu m^4$. To model lumen incompressibility, lumen volume elasticity K_V is such that apical contraction compresses the super-ellipsoid by 5% in volume ($K_V = 1.10^{-5} u/\mu m^6$ (Supplementary Fig 6). Preferred area A_0 and preferred perimeter P_0 are chosen to have a constant $P_0/\sqrt{A_0}$ ratio of 2 throughout the simulation, this corresponds to a stiff tissue in

(Bi et al., 2015) framework. With the above value of $P_0/\sqrt{A_0}$, we choose the apical perimeter elasticity K_p to allow cell shape changes upon apical constriction

Please refers to table S1 for a description of parameters and tested values.

Code availability

The code used for modelling is publicly available: https://github.com/DamCB/tyssue and https://github.com/suzannelab/polarity.

Statistical analysis

523 Mann-Whitney U test was used to evaluate the statistical significance of differences observed
524 between our samples, and computed using Prism 8 (Graph Pad).
525

526 ***Table S1***
527

Parameter Name	Description	Value (value range)	Unit
u	Unit energy term		$pN/\mu m$
	External barrier diameter	100 (130-70)	μm
$\frac{P_0}{\sqrt{A_0}}$	Form factor	2 (1-4)	
K_α	Apical area elasticity	1	$u/\mu m^4$
A_α	Apical area	45	μm^2
$A_{\alpha,0}$	Preferred apical area	45	μm^2
K_p	Apical perimeter elasticity	10 (1-200)	$u/\mu m^4$
$P_{\alpha,0}$	Preferred apical perimeter	13.4	μm
T_α^{ab}	Apical-basal tension for cell α	50 (0-60)	pN
K_b	External barrier elasticity	280	$u/\mu m^4$
R_b	External barrier radius	100 (70-120)	μm
V_0	Preferred lumen volume	1 655 118	μm^3
K_v	Lumen volume elasticity	1.e-5 (1.e-10-1)	$u/\mu m^6$
$\frac{\omega_\perp}{\omega_{//}}$	Polarity	0.5 (0.3-1)	
τ_α	Rate of contractility increase for cell α	1.08 (1.02-1.16)	
$\tau_{\min}$	Rate of contractility increase for farther neighbor cell	1.001	
$r_{\max}$	Span of contractility increase propagation	3	
N_t	Number of time steps for apical-basal traction	30	
r_p	Distance of clone cell form the fold	3	

528
529
530
531 ***Materials and Methods references***

532 Ambrosini, A., Rayer, M., Monier, B., and Suzanne, M. (2019). Mechanical Function of the Nucleus in
533 Force Generation during Epithelial Morphogenesis. Dev Cell *50*, 197-211.e195.
534 Bi, D., Lopez, J.H., Schwarz, J.M., and Manning, M.L. (2015). A density-independent rigidity transition
535 in biological tissues. Nature Physics *11*, 1074-1079.
536 Gracia, M., Theis, S., Proag, A., Gay, G., Benassayag, C., and Suzanne, M. (2019). Mechanical impact of
537 epithelial-mesenchymal transition on epithelial morphogenesis in Drosophila. Nat Commun *10*, 2951.
538 Monier, B., Gettings, M., Gay, G., Mangeat, T., Schott, S., Guarner, A., and Suzanne, M. (2015). Apico-
539 basal forces exerted by apoptotic cells drive epithelium folding. Nature *518*, 245-248.

Schott, S., Ambrosini, A., Barbaste, A., Benassayag, C., Gracia, M., Proag, A., Rayer, M., Monier, B., and Suzanne, M. (2017). A fluorescent toolkit for spatiotemporal tracking of apoptotic cells in living. Development *144*, 3840-3846.

van der Walt, S., Colbert, S.C., and Varoquaux, G. (2011). The NumPy Array: A Structure for Efficient Numerical Computation. Computing in Science and Engineering *13*, 22-30.

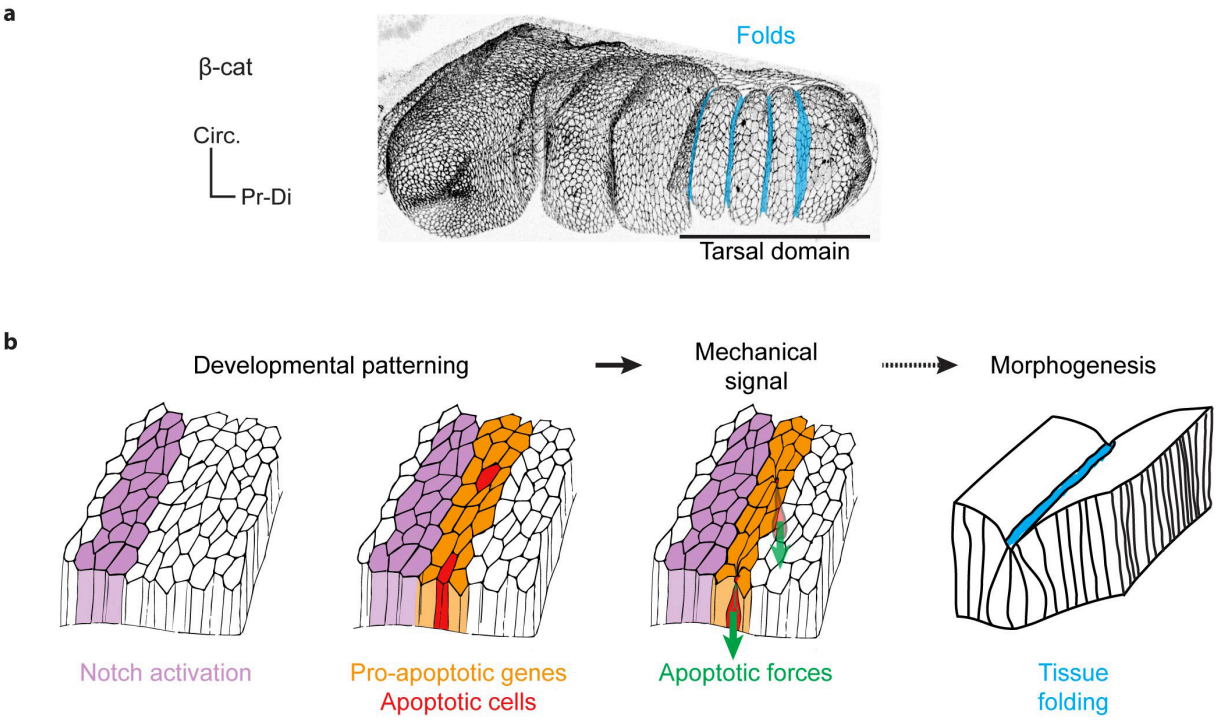

Figure S1: *Drosophila* leg folding (Related to figure 1). a, 3D reconstruction of a leg disc expressing β-catenin (*arm::GFP*) at 1h30 after puparium formation (APF) at 29°C. Parallel folds of the tarsal domain are highlighted in blue. **b,** Schematics recapitulating the processes known to be involved in *Drosophila* leg folding. The sequence of events starts with the activation of Notch signaling pathway (purple) leading to the expression of pro-apoptotic genes in the domain of the future fold (yellow), which increases the susceptibility of cells to die in this specific domain, thus creating the pattern of apoptosis (red cells). Dying cells generate apico-basal forces (green arrows) creating transient deformation of the apical surface of the tissue. These forces are then transmitted to neighboring cells, which change their shape and fold the tissue.

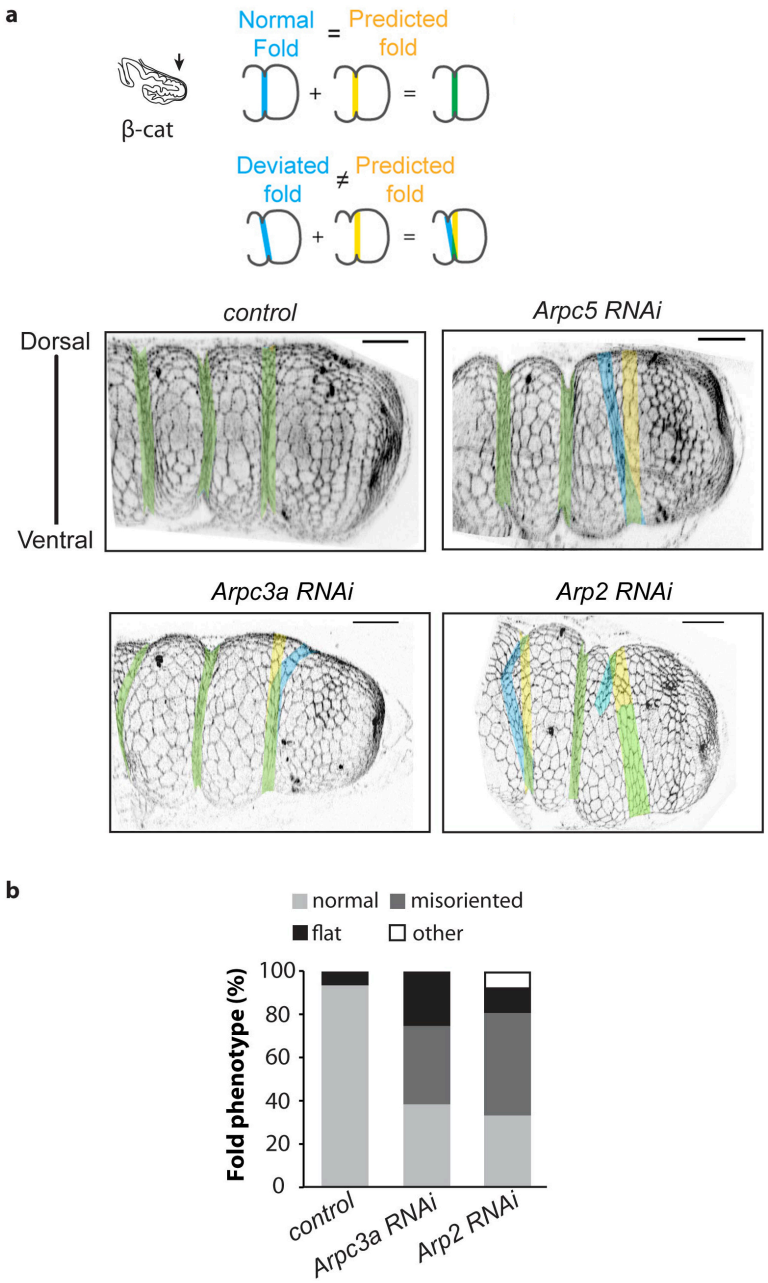

Figure S2: Fold defects in Arp2/3 loss of function contexts (Related to figure 1). a, 3D reconstructions of β-catenin::GFP (*arm::GFP*) leg discs (bottom) and corresponding schematics (top) showing fold phenotypes in *control*, *Arpc5* RNAi, *Arpc3a* RNAi and *Arp2* RNAi animals. Predicted folds are highlighted in yellow, real folds in blue and perfect match between them in green. Scale bar represents 20 µm. **b,** Quantification of T4-T5 fold phenotypes in *control*, *Arpc3a* RNAi and *Arp2* RNAi animals (n=54, 57, 27 legs, respectively). Note that the quantification in the *control* is the same as in Fig.1a.

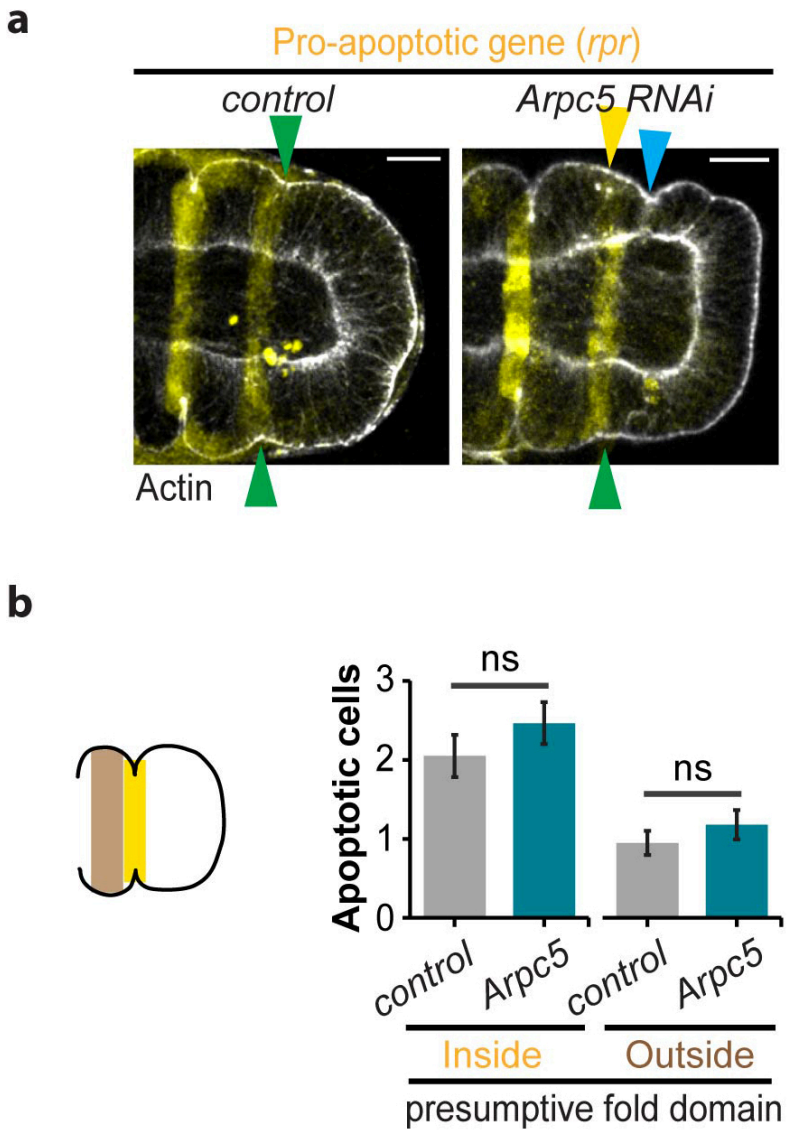

567

568 **Figure S3: Pattern of pro-apoptotic genes and apoptotic cells in Arpc5 knockdown (Related to**
569 **figure 1). a,** Single plane confocal images of *control* (*rpr-lacZ; Dll-Gal4*) or *Arpc5* RNAi (*rpr-lacZ; Dll-*
570 *Gal4; UAS::Arpc5RNAi*) leg stained with phalloidin (white) and showing a Z-projection of rpr-lacZ
571 (yellow). Yellow, blue and green arrowheads respectively indicate predicted fold, real fold and
572 perfect match between them. Scale bar represents 20 µm. **b,** Average number of dying cells inside or
573 outside the predicted distal-most tarsal fold in *control* and *Arpc5* RNAi leg (n=20 and 28 legs,
574 respectively). Bar graphs indicate the mean ± SEM. Statistical significance has been calculated using
575 Mann-Whitney U test. ns, not significant.

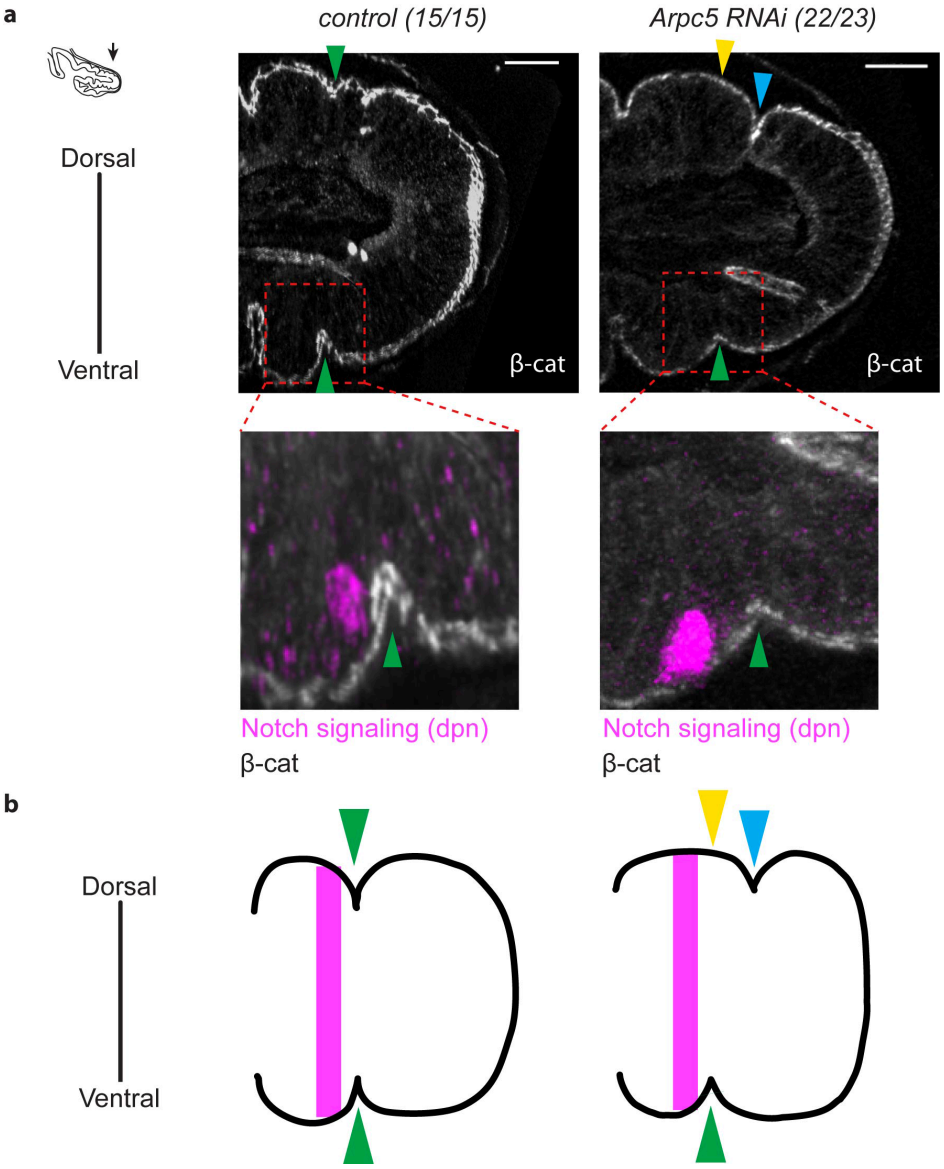

Figure S4: Ventral initiation of folding is correctly located (Related to figure 2). a, Confocal images of *control* (*Dll-Gal4; arm::GFP*) or *Arpc5* RNAi (*Dll-Gal4; arm::GFP, UAS::Arpc5RNAi*) leg discs stained with an anti-deadpan antibody (magenta in the close up views). Scale bar represents 20 µm. Note the correct position of the ventral folding initiation shown in the higher magnifications. **b,** Schematics representing the correct initiation of folding in *Aprc5* RNAi (Right), like in the *control* (left), as shown by the distance between Notch activation domain (magenta) and the fold in the ventral part of the disc. Yellow, blue and green arrowheads respectively indicate predicted fold, real fold and perfect match between them.

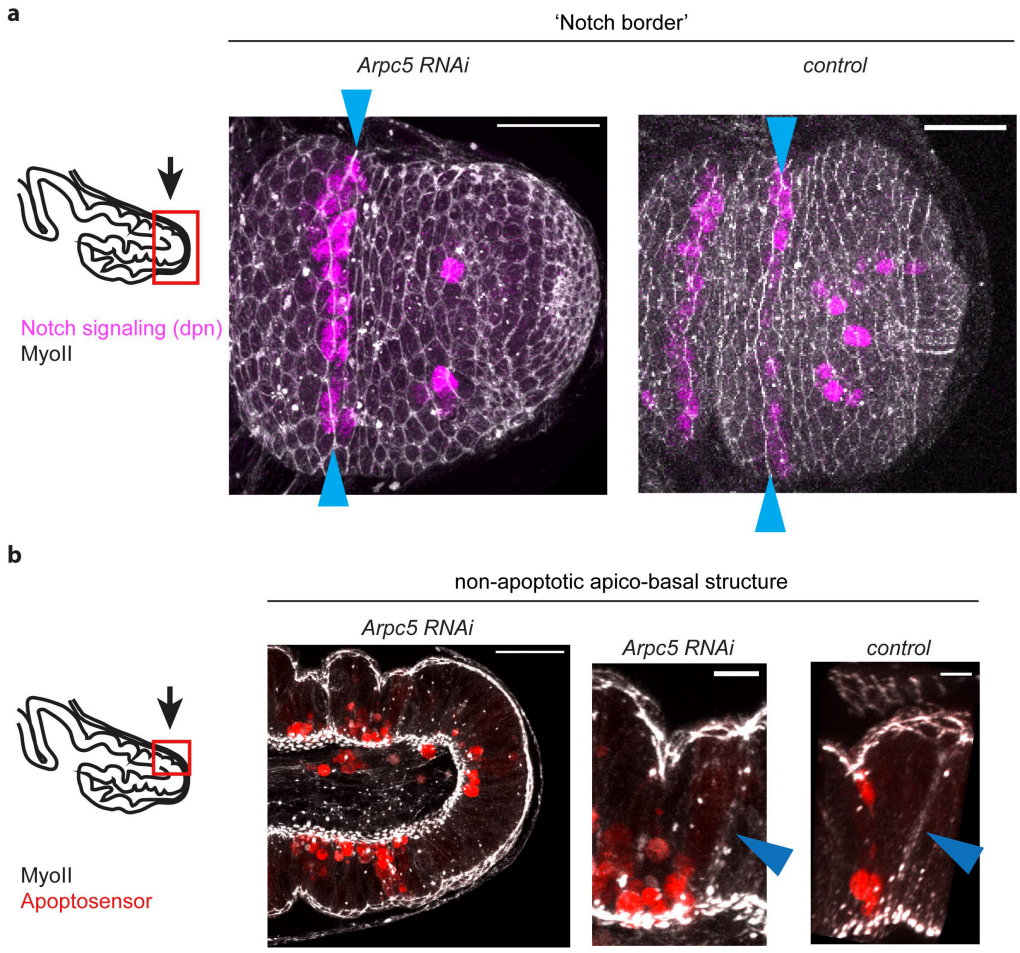

585

586 **Figure S5: Characterization of mechanical perturbations (Related to figure 2). a,** Confocal images of
587 *Arpc5* RNAi (*sqh::GFP[29B]; Dll-Gal4; UAS::Arpc5RNAi*) and *control* (*sqh::GFP[29B]; Dll-Gal4*) leg discs
588 stained with an anti-deadpan antibody (magenta) showing that the supra-cellular cable of myosin is
589 formed at the border of Notch activation domain. Blue arrowheads indicate the Notch activation
590 domain. **b,** Sagittal views of *Arpc5* RNAi (*sqh::RFPt[3B]; Dll-Gal4, UAS::GC3Ai; UAS::Arpc5RNAi*) and
591 *control* (*sqh::RFPt[3B]; Dll-Gal4, UAS::GC3Ai*) leg discs showing that the apico-basal structures of
592 Myosin II observed outside the fold domain (bleu arrowheads) are not related to the presence of
593 apoptotic cells (red).

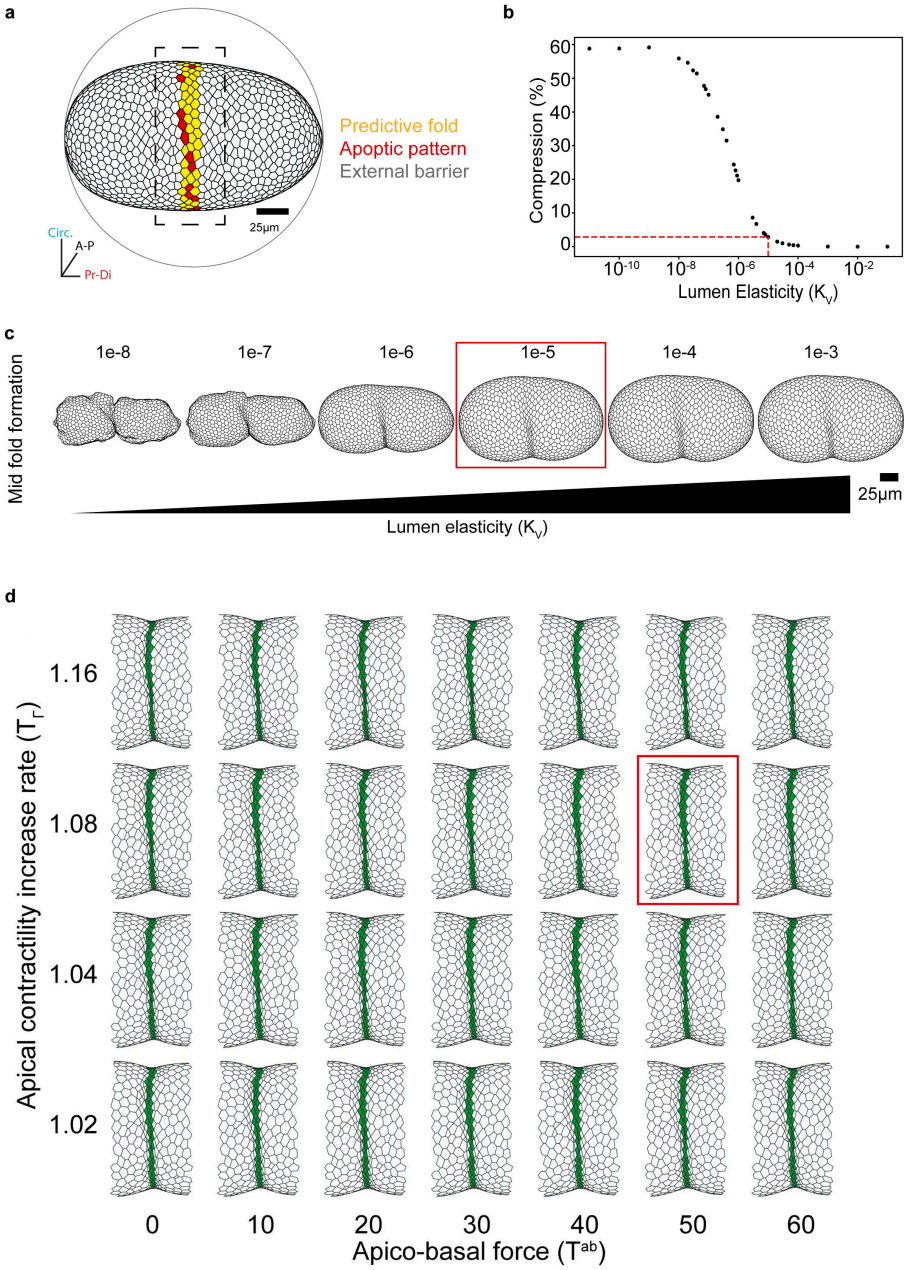

Figure S6: Simulations of epithelium folding. (Related to figure 2). a, Lateral view of the virtual tissue. Cells from the predicted fold domain are indicated in yellow, apoptotic cells in red. The tissue is constrained by a spherical external barrier represented by the grey circle. The black dotted square corresponds to the close-up shown in **d**. **b,** Relative change in the virtual tissue volume as a function of lumen elasticity K^V. Compression is expressed as the ratio between the observed volume and the equilibrium volume V_L^0 *(reprendre les expressions de l'équation 1)*. **c**, aspect of the virtual tissue at maximum fold depth for different values of K^V. Red squared corresponds to the choosen value for K^V. **d,** Simulations obtained at maximal fold depth for distinct values of apical contractility increase rate (y-axis) and apico-basal force (x-axis). All other parameters are unchanged. Fold is in green.

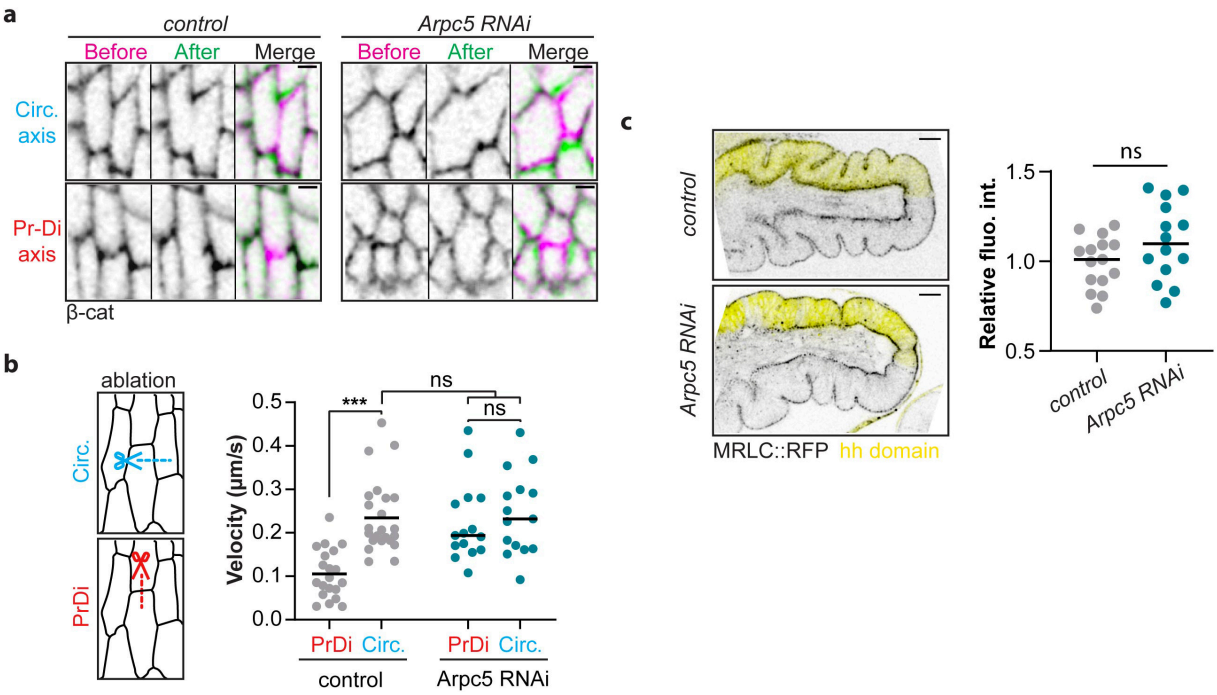

604

605 **Figure S7: Pattern of tension and myosin levels at adherens junctions in Arpc5 knockdown (Related**
606 **to figure 3). a,** Confocal images showing the dynamics of adherens junctions before and after laser
607 ablation of circular (top) and proximo-distal (bottom) junctions in *control* (*Dll-Gal4; arm::GFP*) and
608 *Arpc5 RNAi* (*Dll-Gal4; arm::GFP, UAS::Arpc5RNAi*). **b,** Dot plot showing initial recoil velocity of
609 junctions after laser microdissection in *control* and *Arpc5* RNAi (n=24, 20, 15 and 15 respectively). **c,**
610 Confocal images showing Myosin II distribution in the posterior compartment of control (*sqh::GFP;*
611 *hh-Gal4, UAS-LacZ*) (top, n=15) or *Arpc5* RNAi (*sqh::GFP; hh-Gal4, UAS::Arpc5RNAi*) (bottom ; n=14)
612 legs. The posterior "Hedgehog" domain is highlighted in yellow. Scale bar represents 30 µm. Dot plot
613 showing the relative fluorescence intensity of Myosin II calculated as the ratio between the posterior
614 domain (hh domain, in yellow) and the anterior domain (non yellow).

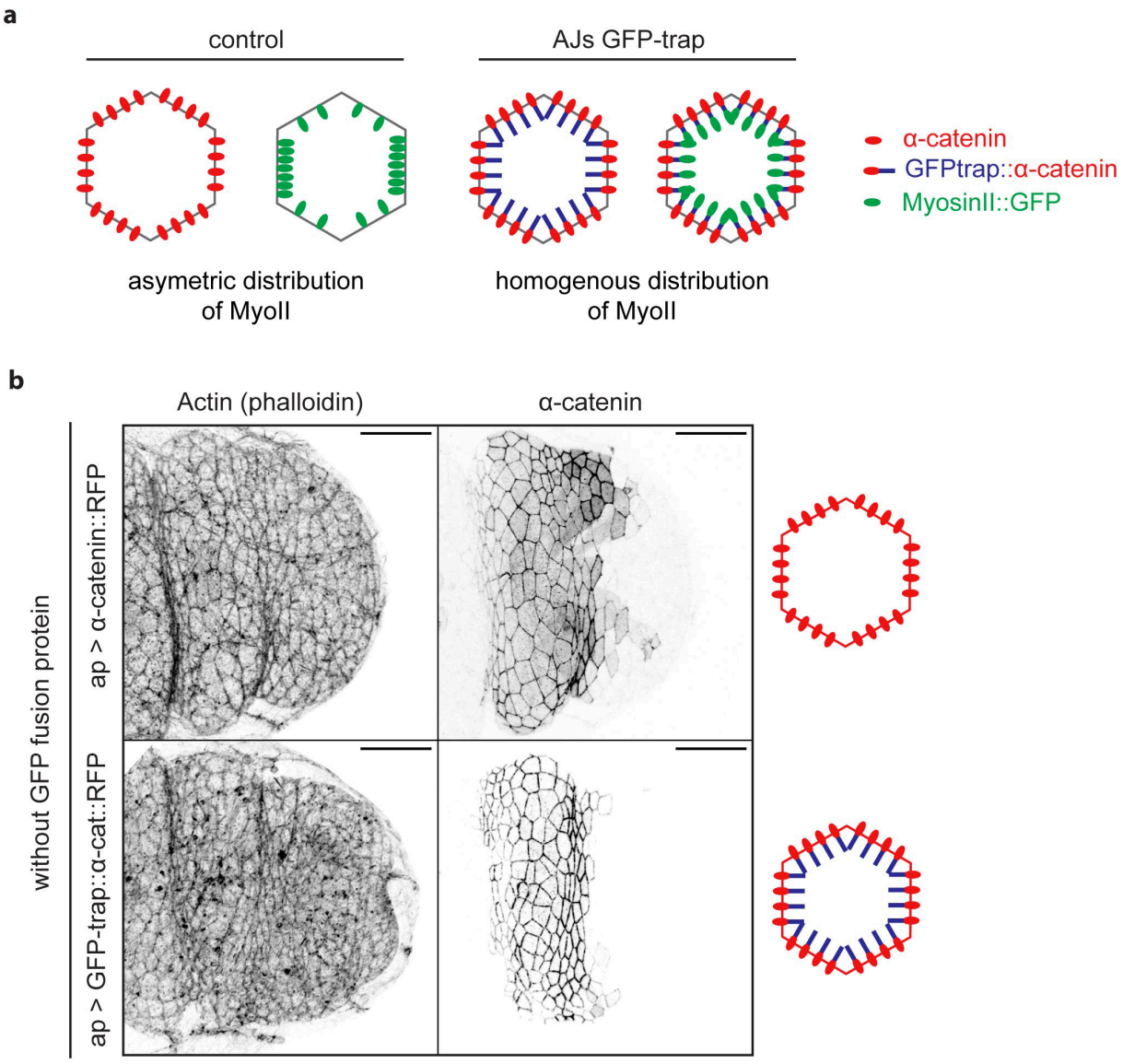

Figure S8: Characterization of the AJs-GFP-trap construct (Related to figure 4). a, Schematics of junctional Myosin II distribution in *control* or GFP-trap context. **b,** Confocal images of *tubG80ts*; *ap-Gal4, UAS-α-catenin::TagRFP* and *tubG80ts; ap-Gal4, UAS-vhhGFP4::α-catenin::TagRFP* legs in absence of GFP fusion protein. The F-actin distribution (phalloidin) shows that the expression of UAS GFP-trap::α-catenin::TagRFP alone does not perturb epithelial organization.

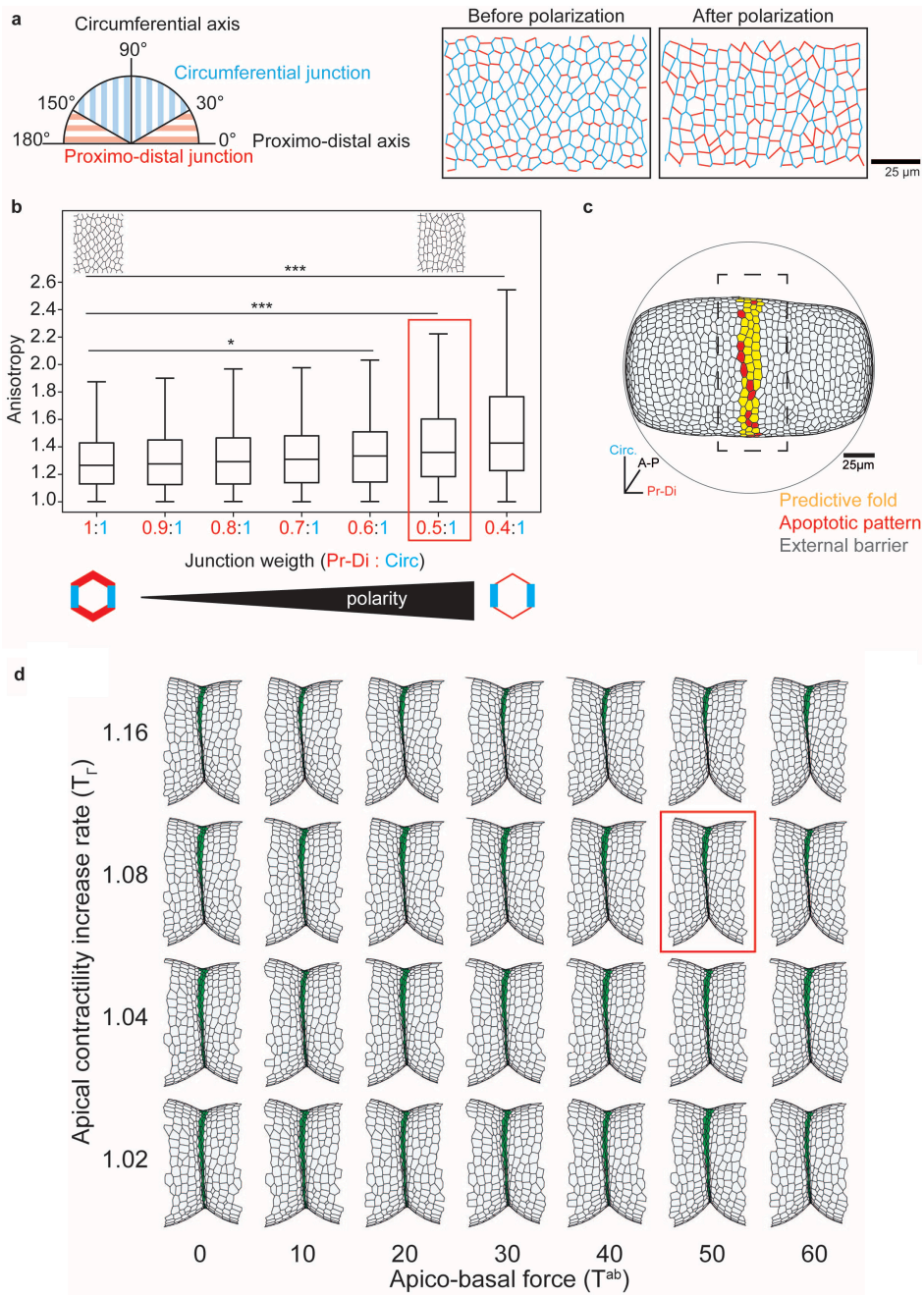

Figure S9: Simulation of fold formation with planar polarity of junctional tension. (Related to figure 4). a, Left panel: Scheme representing the distribution of circumferential and proximo-distal junctions according to their orientation. Bleue junctions are considered oriented in the circumferential axis. Red junctions are considered oriented in the proximo-distal axis. Right panel: repartition of the two types of junctions in the simulation with or without polarization of the tissue. **b,** Box plot presenting the values of tissue anisotropy for different junction weight ratios (weight of proximo-distal junctions/weight of circumferential junctions). The chosen junctional weight ratio is indicated by the red square. Cell shapes are no longer physiological for lower values of weight ratio (data not shown). **c,** Simulation showing the general organization of the polarized tissue before fold formation. Cells from the predicted fold are in yellow, apoptotic cells in red. The tissue is surrounded by a spherical external barrier represented by the grey circle. The black dotted square corresponds to the close-up in panel **d**. **d,** Simulations obtained at maximal fold depth for distinct values of contractility increase rate (y-axis) and apico-basal force (x-axis) with planar polarity. All other parameters are unchanged. Fold is in green.